ACS NANO
Cite This: ACS Nano 2019, 13, 671−680
www.acsnano.org

ARTICLE

Coaxial Carbon Nanotube Supported TiO_2@MoO_2@Carbon Core−Shell Anode for Ultrafast and High-Capacity Sodium Ion Storage

Chunrong Ma,[†,§] Xiang Li,[‡] Changjian Deng,[§] Yan-Yan Hu,[‡] Sungsik Lee,[∥] Xiao-Zhen Liao,[†] Yu-Shi He,[†] Zi-Feng Ma,[*,†,⊥] and Hui Xiong[*,§]

[†]Shanghai Electrochemical Energy Devices Research Centre, School of Chemistry and Chemical Engineering, Shanghai Jiao Tong University, Shanghai 200240, China

[‡]Department of Chemistry & Biochemistry, Florida State University, Tallahassee, Florida 33172, United States

[§]Micron School of Materials Science and Engineering, Boise State University, Boise, Idaho 83725, United States

[∥]Advanced Photon Source, Argonne National Laboratory, Lemont, Illinois 60439, United States

[⊥]Zhejiang Natrium Energy Inc., Shaoxing 312000, China

Supporting Information

ABSTRACT: **The sluggish kinetic in electrode materials is one of the critical challenges in achieving high-power sodium ion storage. We report a coaxial core−shell nanostructure composed of carbon nanotube (CNT) as the core and TiO_2@MoO_2@C as shells for a hierarchically nanoarchitectured anode for improved electrode kinetics. The 1D tubular nanostructure can effectively reduce ion diffusion path, increase electrical conductivity, accommodate the stress due to volume change upon cycling, and provide additional interfacial active sites for enhanced charge storage and transport properties. Significantly, a synergistic effect between TiO_2 and MoO_2 nanostructures is investigated through *ex situ* solid-state nuclear magnetic resonance. The electrode exhibits a good rate capability (150 mAh g^{-1} at 20 A g^{-1}) and superior cycling stability with a reversibly capacity of 175 mAh g^{-1} at 10 A g^{-1} for over 8000 cycles.**

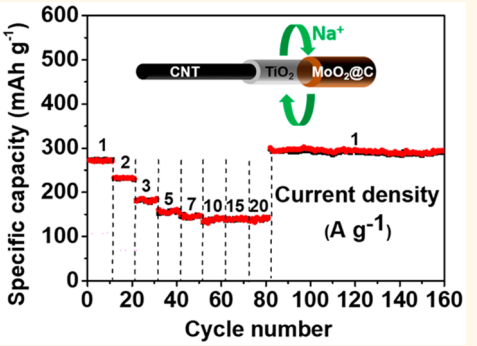

KEYWORDS: *sodium ion storage, hierarchical nanoarchitecture, anode, high rate, long cycle life*

Lithium ion batteries (LIBs), as a leading electrochemical energy storage (EES) technology, have achieved great success in the past few decades for applications such as portable electronics and next-generation electric vehicles.[1−7] Nevertheless, the application of LIBs for large-scale EES for power grids that utilize intermittent renewable energies such as solar and wind is still hampered by limited lithium resources and the surging raw materials cost. Sodium ion battery (SIB) as an alternative to LIB has been proposed as one of the potential and promising technologies for large-scale EES due to its low cost, high abundance, and large availability worldwide.[8,9] However, compared to LIBs, SIBs suffer from more serious issues in power performance and long-term stability, resulting from the sluggish kinetics and large volume change upon cycling due to the much larger Na^+ ion (approximately two times the size of Li^+). To date, for anode materials in SIBs, various alloy-type (*e.g.*, P, Sn, and Sb)[10−12] and conversion-type (*e.g.*, MoS_2, SnS_2, FeP and SnP_3)[13−16] electrode materials have been investigated because of their high theoretical specific capacities. Nevertheless, those materials suffer from poor cycling stability associated with the aforementioned causes. As such, developing an ideal electrode for SIBs that can accommodate the large Na^+ ions reversibly with enhanced kinetics presents a great challenge.

Intercalation-type materials are promising anode candidates as they can reversibly insert/extract Na^+ while maintaining structural integrity. Intercalation-type anode materials such as disordered carbon,[17−20] Ti-based oxide,[21−25] molybdenum dioxide,[26,27] and niobium pentoxide[28−32] have been investigated. Since TiO_2 and titanate were explored as anode materials for SIBs in 2011,[21,33] significant work has been performed toward developing intercalation-type oxide anode

Received: October 12, 2018
Accepted: December 28, 2018
Published: December 28, 2018

DOI: 10.1021/acsnano.8b07811
ACS Nano 2019, 13, 671−680

materials. Tahir and co-workers reported carbon-coated anatase TiO_2 nanostructure with a specific capacity of 125 mAh g^{-1} at a 10 C rate.[34] Chen and co-workers synthesized a TiO_2/graphene composite to enhance the rate capability (~100 mAh g^{-1} at 6 A g^{-1}).[35] Jiang *et al.* have shown a MoO_2/C composite electrode with a capacity of 96 mAh g^{-1} at 3 A g^{-1}.[36] Despite these advances, practical performance of these materials is still not satisfactory for large-scale EES or electric vehicles applications that require high energy/high power. Therefore, it can be quite challenging yet highly desirable to explore an effective strategy for intercalation oxide electrode design to enhance energy density, power density, and cycle life for practical sodium ion storage.

It has been understood that pseudocapacitive charge storage that occurs at the surface of the electrode materials has the advantage of rendering superior high-rate performance and reversibility by shortening the ion diffusion length and electron-transport distance.[37,38] Pseudocapacitive charge storage can be categorized into intrinsic (*e.g.*, RuO_2, MnO_2, and Nb_2O_5) and/or extrinsic (*e.g.*, MoS_2, SnS_2, TiO_2, MoO_2, and V_2O_5) features, where the former is dependent on the nature of materials and the latter results from nanostructuring to maximize reaction sites on the surface.[37,39−45] So far, enhanced pesudocapacitive contribution has been attempted in some alloying-type and conversion-type anode materials,[46,47] and some progress has been made. Zhao and co-workers[46] have reported that the graphene-coupled MoS_2 sandwich-like hybrid delivers 200 mAh g^{-1} at a very high current density of 20 A g^{-1}. Chao and co-workers[47] significantly improved the reversible capacity of SnS by incorporating it with graphene foam to achieve ~1100 mAh g^{-1} at 100 mA g^{-1}. Nevertheless, the exploration of pseudocapacitive charge storage in intercalation oxide electrodes is still limited, where the challenge lies at improving their electrochemistry without sacrificing the host structure stability. Hence, how to maintain structural stability while increasing the capacity (especially at high rates) is critical. It is well accepted that the pseudocapacitive charge storage behavior is concerned with the morphology and particle size of the active materials.[48] Dunn and co-workers[48] have analyzed the impact of the particle size of TiO_2 nanoparticles on pseudocapacitance and concluded that more than 50% pseudocapacitive contribution can be achieved when the particle size is smaller than 10 nm. Therefore, it is feasible to realize high power and energy density in electrode materials by nanoscaling and constructing architectures to maximize the pseudocapacitive contribution.

Herein, we designed a hierarchically architectured anode material where CNT serves as a core to anchor TiO_2 nanoparticles and MoO_2 coating, which is then coated by a layer of N-doped carbon matrix (CNT−TiO_2@MoO_2@C). There are a few advantages of this electrode design: First, the ultrafine nanoparticles can significantly promote the facile access of Na^+/e^-. Second, 1D CNT and N- doped carbon matrix conductive frameworks can facilitate rapid electron and ion transport but concurrently act as the protecting shell to buffer volume changes during repeated cycling. Finally, the interface between TiO_2 and MoO_2 presents a synergistic effect by providing additional sites for charge storage for enhanced energy density. The as-prepared CNT−TiO_2@MoO_2@C exhibits a great rate capability, evidenced by a high capacity of 150 mAh g^{-1} at 20 A g^{-1} and a stable long-cycling performance at 10 A g^{-1} for over 8000 cycles with a reversible capacity of 175 mAh g^{-1}. Furthermore, the charge storage and transport mechanism is investigated utilizing solid-state nuclear magnetic resonance (NMR), cyclic voltammetry (CV), and electrochemical impedance spectroscopy (EIS). Our electrode design strategy may provide a paradigm shift in SIB anode materials for hierarchical structures as well as present insights into a fundamental understanding of the role of interface in hierarchical nanostructures for enhanced performance of SIBs.

RESULTS AND DISCUSSION

Scheme 1 illustrates the detailed preparation of the hierarchical core−shell CNT−TiO_2@MoO_2@C nanocomposite by a two-step method of coating Ti and Mo precursors on CNT and followed by annealing under Ar atmosphere. The structure of pristine CNT is investigated by scanning electron microscopy (SEM) (Figure S1, Supporting Information). In the first step, glucose serves as the structure-directing agent and aromatizes to form hydrophilic functional groups (*e.g.*, hydroxyl and aldehyde groups) on CNT to provide attractive interaction with titanium isopropoxide solution.[49] TiO_2 nanoparticles are formed on CNT where Ti isopropoxide can be hydrolyzed with the presence of trace water. The embedded TiO_2 nanoparticles on CNT (Figure S2, Supporting Information) are crucial for further coating of MoO_2 nanofilm as both glucose aromatization and TiO_2 provide necessary nucleation sites for MoO_2 growth. In the next step, polydopamine−Mo is formed on the surface of CNT−TiO_2 from dopamine polymerization with MoO_4^{2-} under alkaline conditions.[50,51] The derived CNT−TiO_2@Mo-polydopamine compound is subsequently heated at 700 °C to form the final product CNT−TiO_2@MoO_2@C. Compared with pure CNT, the CNT−TiO_2@MoO_2@C nanocomposite preserves the 1D nanostructure (~40−50 nm in diamater) as shown in Figure 1a. Moreover, CNT intertwines with each other to form a network, which could facilitate fast Na^+/e^- transport. The surface of CNT becomes coarse after being coated with TiO_2 and MoO_2, indicating that the surface is covered by densely packed TiO_2@MoO_2 nanoparticles (Figure 1b). The typical coaxial morphology of CNT−TiO_2@MoO_2@C is investigated *via* transmission electron microscopy (TEM). As demonstrated in Figure 1b, the CNTs are encapsulated with the nanocomposites forming the final core/shell structure. A high magnification TEM image (Figure 1c) exhibits that the ultrafine nanoparticles are encapsulated within the carbon matrix to form a robust shell, which can prevent the aggregation of metal oxide nanoparticles and act as a constraint to refrain particles from growing during the annealing process.

Scheme 1. Illustration of the Structure of Coaxial CNT−TiO_2@MoO_2@C

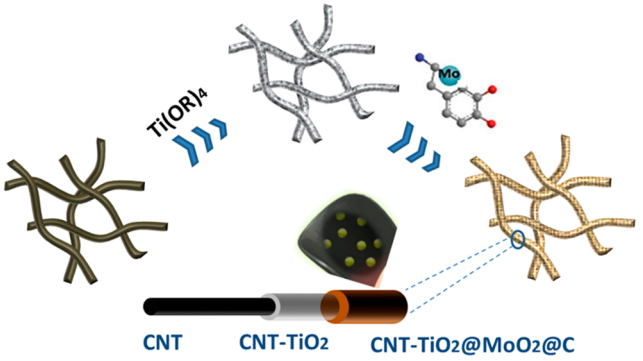

DOI: 10.1021/acsnano.8b07811
ACS Nano 2019, 13, 671−680

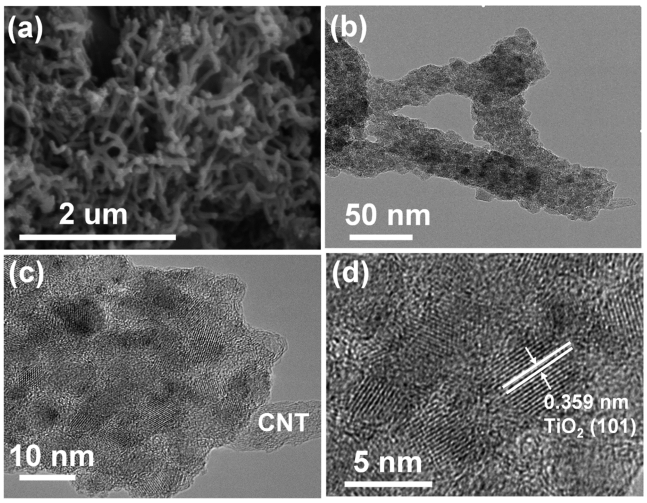

Figure 1. (a) SEM and (b–d) TEM images of the as-prepared CNT–TiO_2@MoO_2@C.

The average oxide particle size of ~5 nm can be observed from the high-resolution TEM (Figure 1d). The d-spacing (0.359 nm) of the lattice fringes shown in Figure 1d is attributed to the (101) plane of anatase TiO_2. Elemental mapping (Figure S3, Supporting Information) using the HAADF-STEM mode shows the elemental distribution of the as-prepared material, which clearly reveals that the Ti, Mo, and C elements are distributed uniformly in the nanocomposite.

The X-ray diffraction (XRD) pattern of the pristine sample is shown in Figure 2a. All of the peaks match well with anatase TiO_2 (JCPDS-21-1272) without distinct MoO_2 diffraction due to the amorphous nature of MoO_2 (Figure S4, Supporting Information). In addition, the as-prepared CNT–TiO_2@MoO_2@C nanocomposite exhibits a relatively high Brunauer–Emmett–Teller (BET) surface area of approximately 125 $m^2\ g^{-1}$ with a typical IV adsorption and desorption isotherms (Figure 2b). The high BET surface area can effectively reduce the Na^+ diffusion distance.

The surface properties and major components of the CNT–TiO_2@MoO_2@C nanocomposite are further examined by XPS. The survey scan spectrum is shown in Figure 3a, which contains C, Ti, Mo, and O elements without any other impurities. From the high-resolution Ti 2p spectrum (Figure 3b), two predominant peaks located at 458.9 and 464.7 eV correspond to the Ti $2p_{3/2}$ and Ti $2p_{1/2}$, respectively. The energy separation between Ti $2p_{3/2}$ and Ti $2p_{1/2}$ peaks is 5.8 eV, which coincides well with Ti^{4+} in anatase TiO_2. From the spectrum of Mo 3d (Figure 3c), it can be divided into two pairs of peaks, and the binding energy of 232.8 and 229.6 eV can be distinguished and ascribed to the $3d_{3/2}$ and $3d_{5/2}$ of Mo^{4+} in MoO_2, while the other two peaks at 235.7 and 230.9 eV could be assigned to the Mo^{6+} in MoO_3 due to surface oxidation.[27] Characterization of MoO_2@C by Raman spectroscopy (Figure S5, Supporting Information) was performed to further support the results above. Several MoO_3 peaks are detected, verifying the Mo^{6+} existence from the oxidation of MoO_2. In addition, to confirm that the majority of the molybdenum oxide in the bulk of CNT–TiO_2@MoO_2@C composite is MoO_2, X-ray absorption near edge structure (XANES) spectrum at Mo K-edge of as-prepared CNT–TiO_2@MoO_2@C sample (Figure S6, Supporting Information) was measured and compared to MoO_2 and MoO_3 standards. The oxidation state of the CNT–TiO_2@MoO_2@C sample was determined to be 4.5 by comparing the inflation point of the main edge of the samples.[52] Thus, it is evident that MoO_2 is the major component of the molybdenum oxide in the nanocomposite, and it could be postulated that MoO_3 mostly remains at the surface. The C 1s spectrum (Figure 3d) is categorized into four peaks: the peak centered at 284.6 eV is considered as the characteristic peak of C–C, whereas the other peaks at 285.3, 286.4, and 290.7 eV can be assigned to C–O, C=O, and O–C=O bonds, respectively.[53] In addition, the molecular ratio of TiO_2 and MoO_2 measured by XPS is 1:1. The thermogravimetric analysis (TGA) is carried out in air to directly evaluate the content of carbon including carbon nanotube and amorphous carbon coating. Figure S7 (Supporting Information) shows a weight change of 3.2% below 250 °C and 13.3% between 250 and 800 °C, which can be attributed to the loss of amorphous carbon and carbon nanotubes, respectively.

The Na^+ storage performance of CNT–TiO_2@MoO_2@C electrode is evaluated in Na half cells. Figure 4a demonstrates the discharge–charge curves at a current density of 500 mA g^{-1} in different cycles (*i.e.*, first, fifth and 100th cycle). The initial discharge and charge capacity was 689 and 352 mAh g^{-1}, yielding a Columbic efficiency of 51.2%. The initial capacity loss can be ascribed to the solid-electrolyte interphase (SEI) film formation as well as electrolyte decomposition.[22,54] Notably, the charge and discharge curves almost overlap during subsequent cycles, which confirms the good structural stability of the CNT–TiO_2@MoO_2@C electrode. The cycling performance of the as-prepared electrode as well as CNT–TiO_2 and MoO_2@C control electrodes are compared at a current rate of 1 A g^{-1} (Figure 4b), which all demonstrate

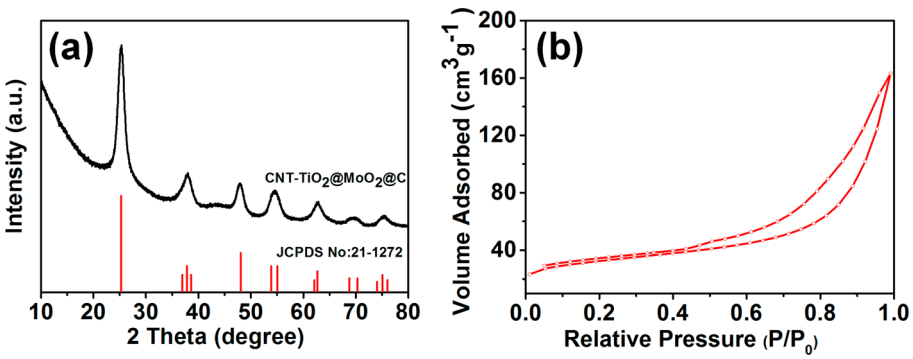

Figure 2. (a) XRD and (b) N_2 adsorption/desorption isotherms of pristine CNT–TiO_2@MoO_2@C sample.

DOI: 10.1021/acsnano.8b07811
ACS Nano 2019, 13, 671–680

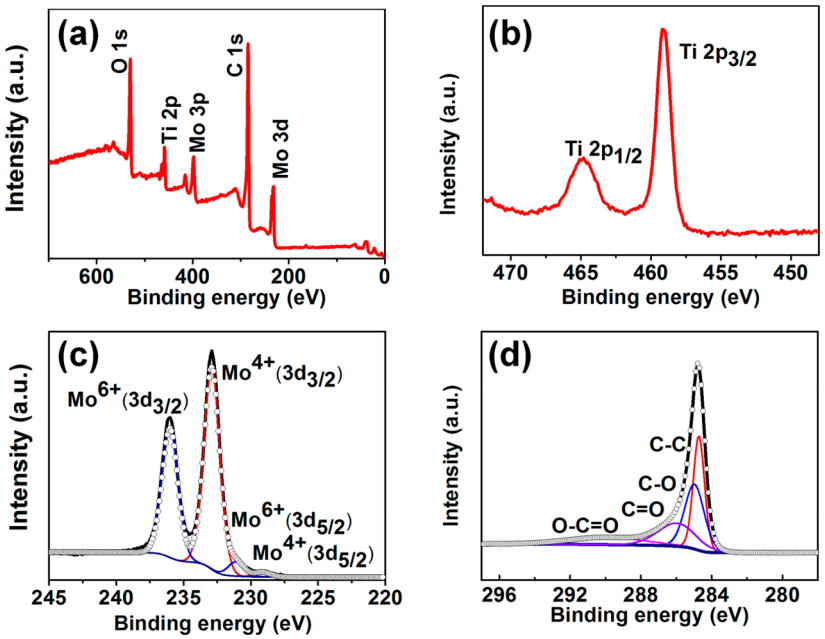

Figure 3. (a) XPS survey scan spectrum of CNT−TiO_2@MoO_2@C. High-resolution XPS of (b) Ti 2p, (c) Mo 3d, and (d) C 1s. Curves with open circles in (c) and (d): fitted results.

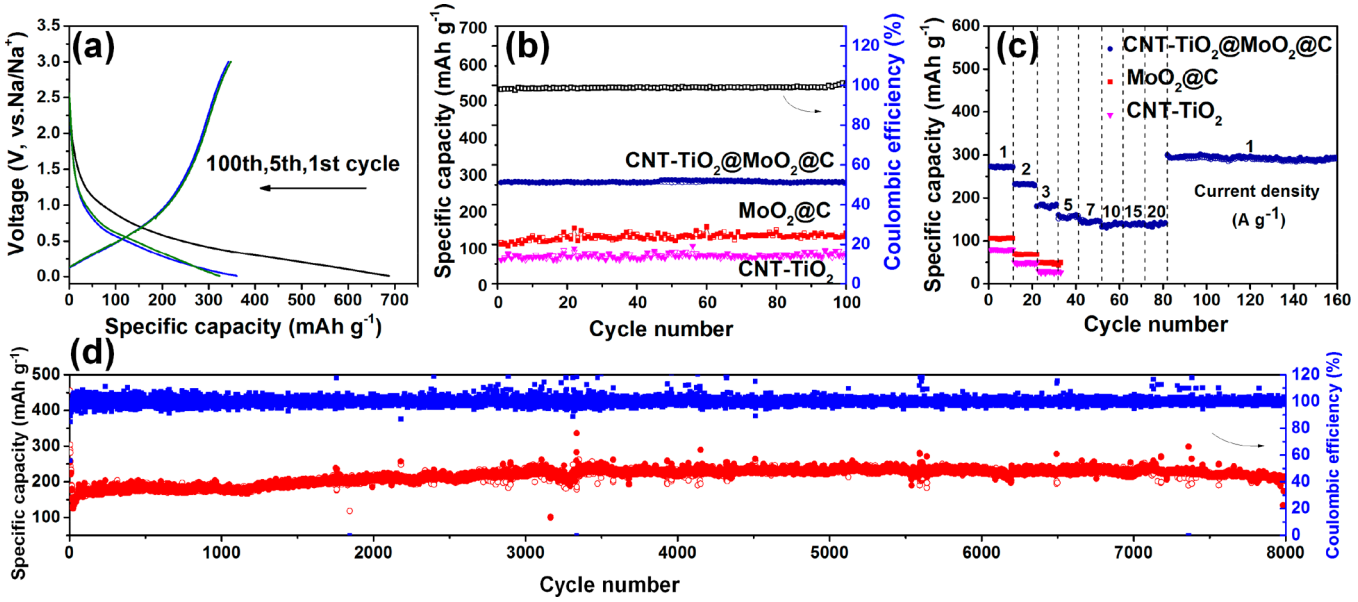

Figure 4. Electrochemical performance of the CNT−TiO_2@MoO_2@C electrode: (a) charge−discharge voltage profiles at a current rate of 500 mA g^{-1} in a potential window of 0.01−3 V, (b) cycling performance of CNT−TiO_2@MoO_2@C, CNT−TiO_2, and MoO_2@C electrodes at a current rate of 1 A g^{-1}, (c) rate capabilities of the CNT−TiO_2@MoO_2@C, CNT−TiO_2, and MoO_2@C electrodes, and (d) cycle life study of the CNT−TiO_2@MoO_2@C electrode at a current rate of 10 A g^{-1}.

good cycling stability. Among all electrodes, CNT−TiO_2@MoO_2@C electrode achieves the highest capacity. It could maintain a discharge capacity of 289 mAh g^{-1} without obvious capacity fading after 100 cycles.

The rate capability of the as-prepared CNT−TiO_2@MoO_2@C electrode is evaluated at various current rates from 1 to 20 A g^{-1} (Figure 4c). As the current rate is increased from 1 to 2, 3, 5, and 7 A g^{-1}, the capacities delivered by the CNT−TiO_2@MoO_2@C electrode decrease slightly from 275 to 225, 187, 153, and 145 mAh g^{-1}. Notably, when the current densities are increased to 10, 15, and 20 A g^{-1}, a capacity of 138 mAh g^{-1} can be achieved and could sustain without obvious decay at increased current densities. Moreover, after the deep charge and discharge cycling at 20 A g^{-1}, the capacity still can be recovered to a reversible capacity of 289 mAh g^{-1} with a Columbic efficiency of ~99.1%. Such superior rate capability offers a strong evidence that the structure of CNT−TiO_2@MoO_2@C is extremely stable, which can accommodate ultrafast charge/discharge cycling and maintain cycling stability. In comparison, the control CNT−TiO_2 and MoO_2@C electrodes only exhibit capacities of 25 and 50 mAh g^{-1} at 3 A g^{-1}, respectively, and the capacities plunge sharply when the current density increases.

DOI: 10.1021/acsnano.8b07811
ACS Nano 2019, 13, 671−680

Long-term cycling stability is critical for practical applications of SIBs. However, Na^+ insertion/extraction in host intercalation materials is significantly hindered due to the larger ionic radius of Na^+ comparing to Li^+. In addition, stress induced from large volume change during cycling leads to structural instability in host materials. The cycle life of the CNT−TiO_2@MoO_2@C electrode is evaluated at a high current rate of 10 A g^{-1} (Figure 4d). Notably, even after 8000 cycles, a high capacity of 175 mAh g^{-1} can be still maintained, implying a reversible and facile Na^+ insertion/extraction due to the efficient ion and electrode transport in the CNT−TiO_2@MoO_2@C electrode. In addition, the Columbic efficiency increases to ∼99−100% after the initial cycles, which implies the highly reversible nature of the electrode. The structural stability of the CNT−TiO_2@MoO_2@C electrode is evaluated by TEM after 1000 cycles (Figure S8, Supporting Information). It can be seen that the overall 1D core−shell structure is almost unchanged and the CNT is coated with TiO_2@MoO_2@C. Such results confirm that the CNT−TiO_2@MoO_2@C electrode is robust enough to accommodate the repeated fast Na^+ intercalation/deintercalation, which are superior to those reported in the literature (Figure 5).[27,34−36,55−59]

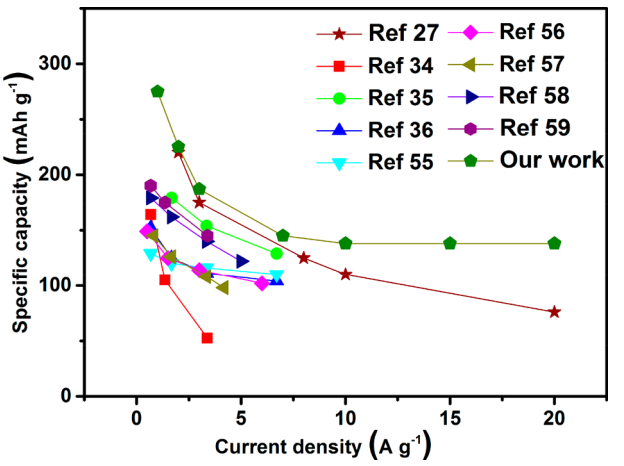

Figure 5. Comparison of the rate performance of CNT−TiO_2@MoO_2@C electrode with electrodes reported in literature (refs 34, 35, and 55−59 are the TiO_2 electrodes; refs 27 and 36 are the MoO_2 electrodes).

To understand the origin of the excellent rate performance, electrochemical impedance spectroscopy (EIS) measurements of the CNT−TiO_2@MoO_2@C, CNT−TiO_2 and MoO_2−C electrodes were conducted, and the corresponding fitted EIS spectra by an equivalent circuit model are shown in Figure 6 (inset). The Nyquist plots (Figure 6a) for these electrodes after 100 cycles at 0.5 A g^{-1} show similar characteristics. In particular, the high and medium-frequency semicircles correspond to SEI associated with a surface process (R_f) and an interfacial charge transfer process (R_{ct}), respectively. In the low frequency region, the straight line is related to the solid-state Li^+ diffusion (Z_w).[60] From the fitted results, the CNT−TiO_2@MoO_2@C electrode exhibits significantly reduced resistance in R_f (34.8 Ω) and R_{ct} (463.7 Ω) compared with those of CNT−TiO_2 (50.8 Ω and 893.1Ω) and MoO_2@C (84.6 Ω and 933.4 Ω) electrodes. The decreased resistance indicates that the CNT−TiO_2@MoO_2@C electrode can effectively facilitate fast ions transfer, which promotes its superior rate capability. Additionally, the Warburg factor (σ) can be obtained by the slope of the Warburg plot (*i.e.*, the real impedance Z' vs the reciprocal of the square root of the angular frequency $\omega^{-1/2}$) (Figure 6b). Apparently, the slope (σ, the Warburg factor) of the CNT−TiO_2@MoO_2@C electrode is smaller than that of the other electrodes, suggesting a higher Na^+ diffusion coefficient in the electrode (σ^2 is inversely proportional to the diffusion coefficient of Na^+).[61] The Na^+ diffusion coefficients from the EIS data can be obtained using following equation[60,61]

$$D_{Na^+} = \frac{R^2T^2}{2A^2n^4F^4C^2\sigma^2} \quad (1)$$

where R is the gas constant, T is the absolute temperature, C is the Na^+ concentration in the electrolyte, n is the transferred charge, F is Faraday's constant, σ is the Warburg factor, and A is the surface area. As shown in Table S1 (Supporting Information), the CNT−TiO_2@MoO_2@C electrode demonstrates a one magnitude larger D_{Na+} than the other electrodes.

The capacitive effect and kinetics of the CNT−TiO_2@MoO_2@C electrode are assessed using CV. Figure 7a presents CVs at a slow scan rate of 0.1 mV s^{-1}. In the first cycle, in addition to two pairs of redox peaks there is a board irreversible peak at around 0.35 V, which is ascribed to SEI formation.[27,60] The peak vanishes in subsequent cycles, which indicates that a stable SEI is formed. The CV curves almost overlap for additional cycles and show two pairs of distinct

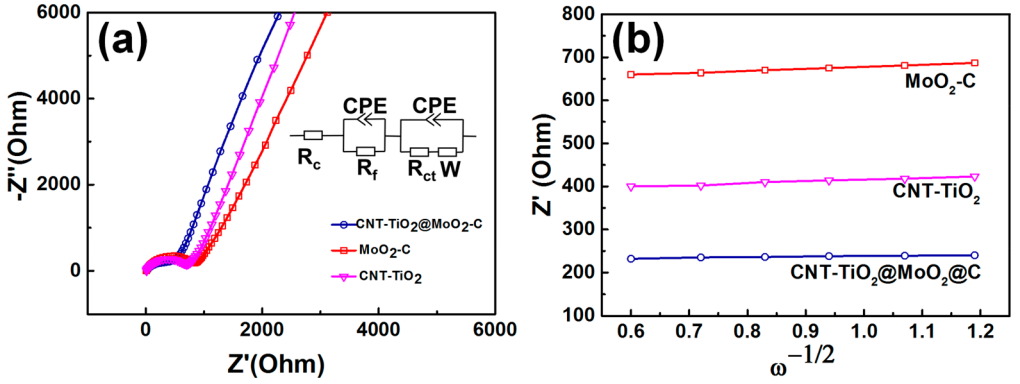

Figure 6. (a) Electrochemical impedance spectra of CNT−TiO_2@MoO_2@C, CNT−TiO_2, and MoO_2@C electrodes (inset: the Randies equivalent circuit model) and (b) real parts of the impedance (Z') *versus* the reciprocal square root of the lower angular frequency (ω).

DOI: 10.1021/acsnano.8b07811
ACS Nano 2019, 13, 671−680

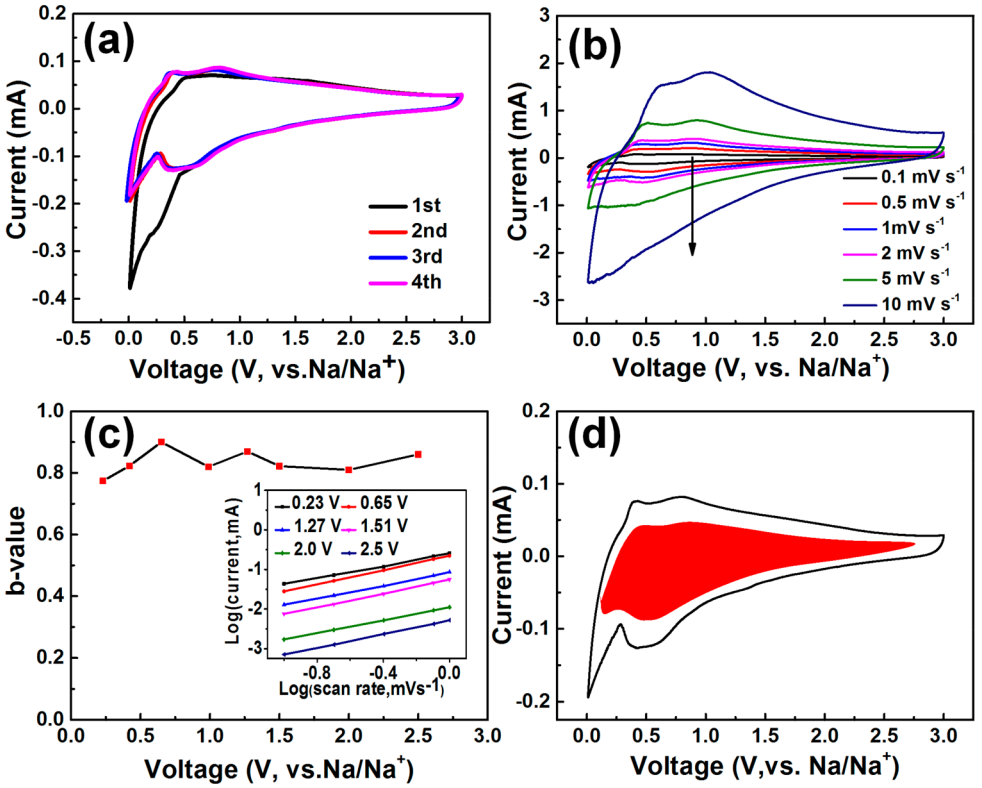

Figure 7. (a) CV curves of CNT−TiO_2@MoO_2@C from the first to fourth cycles at a scan rate of 0.1 mV s^{-1}, (b) CV curves of CNT−TiO_2@MoO_2@C at various sweep rates from 0.1 to 10 mV s^{-1}, (c) *b* values at different voltages during the cathodic scan (inset: current response vs scan rate at different voltages), and (d) capacitive contribution (shaded area) at the scant rate of 0.1 mV s^{-1}.

redox peaks. There is a cathodic peak at∼ 0.62 V, which is related to the reduction of Ti^{4+} to Ti^{3+}.[62] The corresponding oxidation peak is present around 0.78 V. Meanwhile, a redox peak pair (0.35/0.42 V) can be assigned to the Na^+ intercalation/deintercalation in MoO_2,[63] which is in agreement with the CVs of the CNT−TiO_2 and MoO_2@C electrodes (Figure S9, Supporting Information).

To better understand the electrochemical charge storage kinetics of the CNT−TiO_2@MoO_2@C electrode, CVs with various scan rates between 0.1 and 10 mV s^{-1} have been conducted (Figure 7b). The total stored charge may be due to three mechanisms:[48,64,65] faradaic contribution from the Na^+ ion intercalation process, surface pesudocapacitive process, and the nonfaradaic contribution from the double layer effect. The diffusion and capacitive contribution of Na^+ storage can be analyzed by the power law relationship[48,64,65]

$$i = av^b \tag{2}$$

where *i* is the measured current and ν is the scan rate. Both *a* and *b* are adjustable parameters, the value of *b* could be obtained from the slope of log *i* *vs* log *v* plots. In particular, *b* value of 1 implies a capacitive-controlled process.[64] A *b* = 0.5 indicates that the charge storage process is limited by diffusion.[66] As shown in Figure 7c, the *b* values of the CNT−TiO_2@MoO_2@C electrode during the cathodic scan are all above 0.8, indicating Na^+ insertion is mainly from the capacitive process for fast kinetics.[67] In addition, the estimated surface area normalized capacitance is larger than the typical double layer capacitance,[64] indicating the Na^+ storage mechanism on the surface is dominated by pseudocapacitive contribution. Moreover, the diffusion and capacitive contribution to the current response can be quantitatively examined by the following equation[48,64]

$$i = k_1\nu + k_2\nu^{1/2} \tag{3}$$

where the terms $k_1\nu$ and $k_2\nu^{1/2}$ represent the contribution from surface capacitive effect and the diffusion-controlled process, respectively.

As illustrated in Figure 7d, ∼65% the charge storage is from the pseudocapacitive contribution at a scan rate of 0.1 mV s^{-1}. The diffusion contribution is mainly localized at around the redox peaks. From the analysis of voltammetric responses, we propose that the CNT−TiO_2@MoO_2@C electrode facilitates faradaic surface reactions, which promote fast reaction kinetics for excellent rate capability.

It is crucial to understand the exact impact of ion dynamics and active sites of the CNT−TiO_2@MoO_2@C electrode on the obtained electrochemical properties. Therefore, the paramagnetic nature of the TiO_2 and MoO_2 in the CNT−TiO_2@MoO_2−C composite is analyzed by the solid-state nuclear magnetic resonance (NMR). Experimental ^{23}Na NMR spectra of CNT−TiO_2 and MoO_2@C control electrodes discharged to 0.01 V are shown in Figure 8a, along with the corresponding simulated spectra. After discharged to 0.01 V, a large amount of Na is inserted into MoO_2 and TiO_2 structures, and the obtained capacities from bare TiO_2 and MoO_2 are 335 mAh^{-1} and 209 mAh g^{-1}, respectively. The ^{23}Na NMR sensitivity for the same amount of Na in CNT−TiO_2 is relatively lower compared to that in MoO_2@C. This is due to different properties of CNT−TiO_2 and MoO_2@C electrodes. TiO_2 is coated on conductive CNTs, which compromises the efficiency of NMR radio frequency pulses, leading to reduced

DOI: 10.1021/acsnano.8b07811
ACS Nano 2019, 13, 671−680

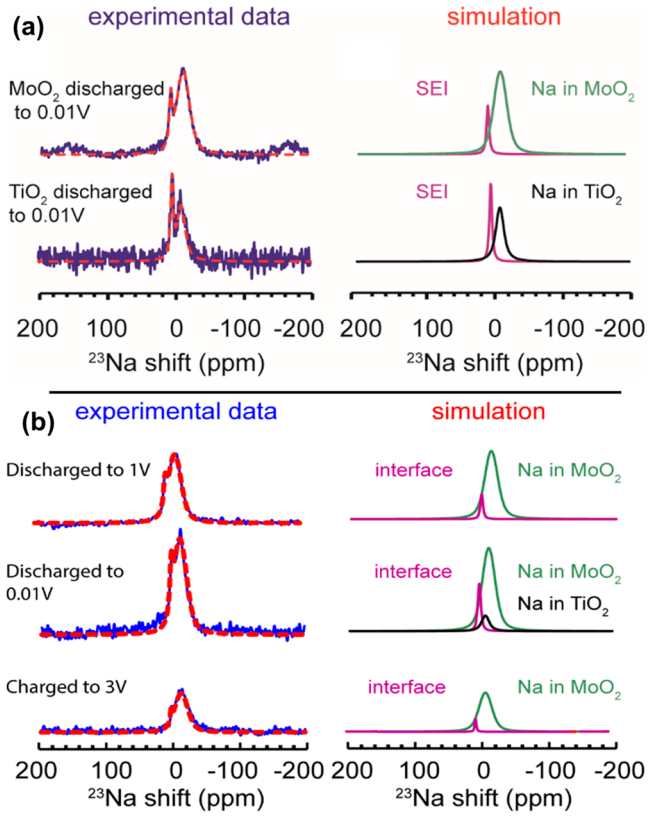

Figure 8. (a) Experimental and simulated ^{23}Na NMR spectra of MoO_2 and TiO_2 electrodes discharged to 0.01 V and (b) experimental and simulated ^{23}Na NMR spectra of CNT−TiO_2@MoO_2@C electrodes at different states of charge.

detection sensitivity of Na in TiO_2. Therefore, a scaling factor of 3.09 is introduced to make the results quantitative based on calibration. The ^{23}Na resonance at −11.9 ppm is assigned to Na inserted into MoO_2 and the peak around −7 ppm is attributed to Na in TiO_2. A resonance around 6.6 ppm is observed in the spectra of both cycled TiO_2 and MoO_2 electrodes, which is from SEI, formed due to electrolyte decomposition at low voltages.

Experimental and simulated ^{23}Na NMR spectra acquired on CNT−TiO_2@MoO_2@C samples at different states of charge are shown in Figure 8b, respectively. In addition to ^{23}Na resonance from Na in MoO_2 (−12.0 ppm) and in TiO_2 (−7.0 ppm), a new resonance around 2.6 ppm is assigned to Na at the interface between MoO_2 and TiO_2, of which the amount increases during discharge and decreases during charge. Na in MoO_2 is seen in all three states of charge. It is worth noting that Na in TiO_2 is only observed when samples are discharged to 0.01 V, suggesting that Na first inserts into MoO_2 and the MoO_2−TiO_2 interface before into TiO_2. This process is reversible upon charge. Quantitative analysis reveals that the Na distribution is 64% Na in MoO_2, 27% Na in TiO_2 and 9% Na at MoO_2−TiO_2 interface at the end of discharge. It is possible that the Na amount at MoO_2−TiO_2 interface is underestimated, due to the presence of conductive carbon on the TiO_2 surface. Because of the complex structure of interface, the exact quantification is challenging. The upper limit of interfacial Na is 21% of total Na in CNT−TiO_2@ MoO_2.

CONCLUSION

In summary, the hierarchical core−shell structured CNT−TiO_2@MoO_2@C was successfully fabricated using CNT as the core. The 1D coaxial-shaped structure could facilitate efficient electron/ion transport. In specific, the TiO_2@MoO_2 nanoparticles encapsulate in the carbon matrix and preferentially assemble into the sandwich-like structure between the CNT and the carbon outer layer, which could improve the conductivity and stability of the nanocomposite as well as serve as the constraint to restrict the growth of the active particles and protect them from attack by the electrolyte. Results from EIS and CV of various scan rates suggest that CNT−TiO_2@MoO_2@C electrode has enhanced kinetics in charge transfer and transport, which are associated with its hierarchical nanoarchitecture and high pseudocapacitance contribution. Interestingly, solid-state NMR study shows that in addition to the active sites in TiO_2 and MoO_2 the interface between TiO_2 and MoO_2 acts an importance role for additional charge storage, which highlights the importance for interface design. Based on the hierarchical nanoarchitecture design and the synergistic effects between TiO_2 and MoO_2, the CNT−TiO_2@MoO_2@C electrode demonstrates an excellent rate capability of 289 mAh g^{-1} at 1 A g^{-1} and 150 mAh g^{-1} at 20 A g^{-1}, which is superior to all of the previous reported Ti and Mo-based anodes in SIBs. More importantly, an ultralong cycle life as over 8000 cycles is achieved in this electrode. The present work suggests that rational design of nanostructures can be an effective way to obtain long-life and ultrafast sodium ion storage.

METHODS

Material Preparation. First, the CNT−TiO_2 precursor was synthesized using a solvothermal method. The mixture of 1 mL of titanium isopropoxide, 0.3 g of glucose, and 35 mg of multiwalled carbon nanotubes (CNT, XFNANO Co., Ltd.) were added in 30 mL of ethanol and sonicated for 1 h. The obtained dispersed solution was heated to 180 °C and maintained for 24 h in a Teflon-lined stainless steel autoclave. The precipitates were centrifuged with ethanol and water several times and then dried at 50 °C. Second, 0.15 g of CNT−TiO_2 was dispersed into a solution of 80 mL of water and 150 mL of ethanol, and 0.15 mg of dopamine and 0.8 g of ammonium molybdate were added into the solution. Subsequently, ammonium hydrochloride was injected until the pH reached to 8, and the reaction was kept for 3 h under ambient conditions.[27] The product was further harvested by high-speed centrifugation. To obtain the final product, the as-prepared precursor was calcined at 700 °C for 2 h under Ar atmosphere. In order to compare the performance, control CNT−TiO_2 and MoO_2@C samples were synthesized using the same conditions without Mo and Ti sources, respectively.

Material Characterization. XRD was recorded by a Bruker D8 diffractometer (Bruker) with a Cu Kα X-ray source (λ = 1.5418 Å). SEM images were collected by a Sirion 200 (FEI Co.) at an acceleration voltage of 15 kV. TEM images were obtained by a JEM-2100F (JEOL) with an accelerating voltage of 200 kV. XPS spectra were acquired by a ESCALAB 250. Raman spectra were collected by a LabRAM HR800 utilizing a 780 nm laser. The surface areas of the samples were performed using the nitrogen adsorption−desorption isotherms (an Autosorb 6B instrument) at 77 K. Bruker Avance III spectrometer was used to examine ^{23}Na magic-angle-spinning (MAS) NMR in a 14.1 T magnetic field with a ^{23}Na Larmor frequency of 132.34 MHz. Electrodes were packed into 2.5 mm rotors and spun at a MAS rate of 25 kHz. The one-pulse sequence was employed, the recycle delay was 100 s, and the 90° pulse length was 2 μs. One M $NaCl_{(l)}$ with a ^{23}Na chemical shift at 0 ppm was used as the shift reference. Synchrotron X-ray absorption near edge structure measurements were carried out at beamline 12BM-B (Advanced Photon

DOI: 10.1021/acsnano.8b07811
ACS Nano 2019, 13, 671−680

Source, Argonne National Laboratory). Mo K-edge spectra were measured at ambient temperature in transmission mode between 19.7995 and 20.8531 keV in steps of about 1.2 eV. Data merging, calibration/alignment, analysis and peak fitting were performed with the Athena program. The Mo K-edge is calibrated to the reference Mo metal foils by setting the first maximum in the derivative plot of absorption *versus* energy equal to the standard electron-binding energy.

Electrochemical Measurements. The 2016-type coin cells were assembled in a dry glovebox (O_2 < 0.1 ppm). The working electrode was composed of 80% active material, 10% super P, and 10% CMC. The testing cell was made of the working electrode, counter and reference electrode (sodium metal), a separator, and the electrolyte using 1 M $NaClO_4$ in the mixture of EC/PC (1:1). Galvanostatic charge−discharge measurements were conducted by a Land battery cycler. CV tests were performed at a scan rate from 0.1 to 5 mV s^{-1} using a CHI605D electrochemical workstation. EIS was recorded on AUTOLAB.

ASSOCIATED CONTENT

Supporting Information

The Supporting Information is available free of charge on the ACS Publications website at DOI: 10.1021/acsnano.8b07811.

TEM of CNT−TiO_2; SEM of CNT; Ti, Mo, and C EDX mapping; XRD of the MoO_2@C; Raman of the MoO_2@C; XANES; TGA of CNT−TiO_2@MoO_2@C; TEM of the CNT−TiO_2@MoO_2@C electrode after 1000 cycles; CV of CNT−TiO_2 and MoO_2@C (PDF)

AUTHOR INFORMATION

Corresponding Authors

*E-mail: clairexiong@boisestate.edu.
*E-mail: zfma@sjtu.edu.cn.

ORCID

Yan-Yan Hu: 0000-0003-0677-5897
Hui Xiong: 0000-0003-3126-1476

Notes

The authors declare no competing financial interest.

ACKNOWLEDGMENTS

H.X. and C.D. acknowledge support by the National Science Foundation under Grant No. DMR-1454984. This work was also supported by the National Natural Science Foundation of China (21676165), and the Shanghai Natural Science Foundation (15ZR1422300). This research used resources of the Advanced Photon Source, a U.S. Department of Energy (DOE) Office of Science User Facility operated for the DOE Office of Science by Argonne National Laboratory under Contract No. DE-AC02-06CH11357.

REFERENCES

(1) Zhou, H. S. New Energy Storage Devices for Post Lithium-Ion Batteries. *Energy Environ. Sci.* **2013**, *6*, 2256−2256.
(2) Lee, S. Y.; Choi, K. H.; Choi, W. S.; Kwon, Y. H.; Jung, H. R.; Shin, H. C.; Kim, J. Y. Progress in Flexible Energy Storage and Conversion Systems, With A Focus on Cable-Type Lithium-Ion Batteries. *Energy Environ. Sci.* **2013**, *6*, 2414−2423.
(3) Cong, L. N.; Xie, H. M.; Li, J. H. Hierarchical Structures Based on Two-Dimensional Nanomaterials for Rechargeable Lithium Batteries. *Adv. Energy Mater.* **2017**, *7*, 1601906.
(4) Sun, Y. M.; Liu, N. A.; Cui, Y. Promises and Challenges Of Nanomaterials for Lithium-Based Rechargeable Batteries. *Nat. Energy.* **2016**, *1*, 16071.
(5) Liu, H. K.; Wang, G. X.; Guo, Z. P.; Wang, J. Z.; Konstantinov, K. Nanomaterials for Lithium-Ion Rechargeable Batteries. *J. Nanosci. Nanotechnol.* **2006**, *6*, 1−15.
(6) Massé, R. C.; Liu, C. F.; Li, Y. W.; Mai, L. Q.; Cao, G. Z. Energy Storage Through Intercalation Reactions: Electrodes for Rechargeable Batteries. *Natl. Sci. Rev.* **2016**, *4*, 26−53.
(7) Rolison, D. R.; Nazar, L. F. Electrochemical Energy Storage to Power The 21st Century. *MRS Bull.* **2011**, *36*, 486−493.
(8) Lu, X. C.; Li, G. S.; Kim, J. Y.; Mei, D. H.; Lemmon, J. P.; Sprenkle, V. L.; Liu, J. Liquid-Metal Electrode to Enable Ultra-Low Temperature Sodium-Beta Alumina Batteries for Renewable Energy Storage. *Nat. Commun.* **2014**, *5*, 4578.
(9) Kundu, D.; Talaie, E.; Duffort, V.; Nazar, L. F. The Emerging Chemistry of Sodium Ion Batteries for Electrochemical Energy Storage. *Angew. Chem., Int. Ed.* **2015**, *54*, 3431−3448.
(10) Zhao, Y. B.; Manthiram, A. High-Capacity, High-Rate Bi-Sb Alloy Anodes for Lithium-Ion and Sodium-Ion Batteries. *Chem. Mater.* **2015**, *27*, 3096−3101.
(11) Xie, X. Q.; Kretschmer, K.; Zhang, J. Q.; Sun, B.; Su, D. W.; Wang, G. X. Sn@CNT Nanopillars Grown Perpendicularly on Carbon Paper: A Novel Free-Standing Anode for Sodium Ion Batteries. *Nano Energy* **2015**, *13*, 208−217.
(12) Liu, S.; Feng, J. K.; Bian, X. F.; Liu, J.; Xu, H.; An, Y. L. A Controlled Red Phosphorus@Ni-P Core@Shell Nanostructure As An Ultralong Cycle-Life and Superior High-Rate Anode for Sodium-Ion Batteries. *Energy Environ. Sci.* **2017**, *10*, 1222−1233.
(13) Li, W. J.; Chou, S. L.; Wang, J. Z.; Liu, H. K.; Dou, S. X. A New, Cheap, and Productive Fep Anode Material for Sodium-Ion Batteries. *Chem. Commun.* **2015**, *51*, 4720−4720.
(14) Fan, X. L.; Mao, J. F.; Zhu, Y. J.; Luo, C.; Suo, L. M.; Gao, T.; Han, F. D.; Liou, S. C.; Wang, C. S. Superior Stable Self-Healing SnP_3 Anode for Sodium-Ion Batteries. *Adv. Energy Mater.* **2015**, *5*, 1500174.
(15) Zhu, C. B.; Kopold, P.; Li, W. H.; Van Aken, P. A.; Maier, J.; Yu, Y. A General Strategy to Fabricate Carbon-Coated 3D Porous Interconnected Metal Sulfides: Case Study of SnS/C Nanocomposite for High-Performance Lithium and Sodium Ion Batteries. *Adv. Sci.* **2015**, *2*, 1500200.
(16) David, L.; Bhandavat, R.; Singh, G. MoS_2/Graphene Composite Paper for Sodium-Ion Battery Electrodes. *ACS Nano* **2014**, *8*, 1759−1770.
(17) Bommier, C.; Surta, T. W.; Dolgos, M.; Ji, X. New Mechanistic Insights on Na-Ion Storage in Nongraphitizable Carbon. *Nano Lett.* **2015**, *15*, 5888−5892.
(18) Zhou, D.; Peer, M.; Yang, Z.; Pol, V. G.; Key, F. D.; Jorne, J.; Foley, H. C.; Johnson, C. S. Long Cycle Life Microporous Spherical Carbon Anodes for Sodium-Ion Batteries Derived from Furfuryl Alcohol. *J. Mater. Chem. A* **2016**, *4*, 6271−6275.
(19) Sun, D.; Kwon, C. W.; Baure, G.; Richman, E.; Maclean, J.; Dunn, B.; Tolbert, S. H. The Relationship Between Nanoscale Structure and Electrochemical Properties of Vanadium Oxide Nanorolls. *Adv. Funct. Mater.* **2004**, *14*, 1197−1204.
(20) Smith, K.; Parrish, R.; Wei, W.; Liu, Y.; Li, T.; Hu, Y. H.; Xiong, H. Disordered 3 D Multi-Layer Graphene Anode Material from CO_2 For Sodium-Ion Batteries. *ChemSusChem* **2016**, *9*, 1397−1402.
(21) Xiong, H.; Slater, M. D.; Balasubramanian, M.; Johnson, C. S.; Rajh, T. Amorphous TiO_2 Nanotube Anode for Rechargeable Sodium Ion Batteries. *J. Phys. Chem. Lett.* **2011**, *2*, 2560−2565.
(22) Mao, M. L.; Yan, F. L.; Cui, C. Y.; Ma, J. M.; Zhang, M.; Wang, T. H.; Wang, C. S. Pipe-Wire TiO_2-Sn@Carbon Nanofibers Paper Anodes For Lithium and Sodium Ion Batteries. *Nano Lett.* **2017**, *17*, 3830−3836.
(23) Li, Y. W.; Chen, C. C.; Wang, M. Y.; Li, W. Q.; Wang, Y. J.; Jiao, L. F.; Yuan, H. T. Excellent Sodium Storage Performance Of Carbon-Coated TiO_2: Assisted With Electrostatic Interaction of Surfactants. *J. Power Sources* **2017**, *361*, 326−333.
(24) Wu, F.; Luo, R.; Xie, M.; Li, L.; Zhang, X. X.; Zhao, L. Z.; Zhou, J. H.; Wang, K. K.; Chen, R. J. Facile Synthesis of Carbon-Mediated Porous Nanocrystallite Anatase TiO_2 for Improved Sodium

DOI: 10.1021/acsnano.8b07811
ACS Nano 2019, 13, 671−680

Insertion Capabilities As An Anode for Sodium-Ion Batteries. *J. Power Sources* **2017**, *362*, 283−290.
(25) Ling, L. M.; Bai, Y.; Wang, Z. H.; Ni, Q.; Chen, G. H.; Zhou, Z. M.; Wu, C. Remarkable Effect of Sodium Alginate Aqueous Binder On Anatase TiO_2 As High-Performance Anode in Sodium Ion Batteries. *ACS Appl. Mater. Interfaces* **2018**, *10*, 5560−5568.
(26) Jiang, J. X.; Yang, W. L.; Wang, H.; Zhao, Y.; Guo, J.; Zhao, J. Q.; Beidaghi, M.; Gao, L. J. Electrochemical Performances of MoO_2/C Nanocomposite for Sodium Ion Storage: An Insight Into Rate Dependent Charge/Discharge Mechanism. *Electrochim. Acta* **2017**, *240*, 379−387.
(27) Zhao, C. T.; Yu, C.; Zhang, M. D.; Huang, H. W.; Li, S. F.; Han, X. T.; Liu, Z. B.; Yang, J.; Xiao, W.; Liang, J. N.; Sun, X. L.; Qiu, J. S. Ultrafine MoO_2-Carbon Microstructures Enable Ultralong-Life Power-Type Sodium Ion Storage By Enhanced Pseudocapacitance. *Adv. Energy Mater.* **2017**, *7*, 1602880.
(28) Yang, L. P.; Zhu, Y. E.; Sheng, J.; Li, F.; Tang, B.; Zhang, Y.; Zhou, Z. T-Nb_2O_5/C Nanofibers Prepared Through Electrospinning With Prolonged Cycle Durability for High-Rate Sodium-Ion Batteries Induced by Pseudocapacitance. *Small* **2017**, *13*, 1702588.
(29) Li, H. S.; Zhu, Y.; Dong, S. Y.; Shen, L. F.; Chen, Z. J.; Zhang, X. G.; Yu, G. H. Self-Assembled Nb_2O_5 Nanosheets for High Energy-High Power Sodium Ion Capacitors. *Chem. Mater.* **2016**, *28*, 5753−5760.
(30) Kim, H.; Lim, E.; Jo, C.; Yoon, G.; Hwang, J.; Jeong, S.; Lee, J.; Kang, K. Ordered-Mesoporous Nb_2O_5/Carbon Composite As A Sodium Insertion Material. *Nano Energy* **2015**, *16*, 62−70.
(31) Yan, L. T.; Chen, G.; Sarker, S.; Richins, S.; Wang, H. Q.; Xu, W. C.; Rui, X. H.; Luo, H. M. Ultrafine Nb_2O_5 Nanocrystal Coating on Reduced Graphene Oxide As Anode Material For High Performance Sodium Ion Battery. *ACS Appl. Mater. Interfaces* **2016**, *8*, 22213−22219.
(32) Wang, L.; Bi, X. F.; Yang, S. B. Partially Single-Crystalline Mesoporous Nb_2O_5 Nanosheets in Between Graphene for Ultrafast Sodium Storage. *Adv. Mater.* **2016**, *28*, 7672.
(33) Senguttuvan, P.; Rousse, G.; Seznec, V.; Tarascon, J.-M.; PalacÍN, M. R. $Na_2Ti_3O_7$: Lowest Voltage Ever Reported Oxide Insertion Electrode for Sodium Ion Batteries. *Chem. Mater.* **2011**, *23*, 4109−4111.
(34) Tahir, M. N.; Oschmann, B.; Buchholz, D.; Dou, X.; Lieberwirth, I.; Panthöfer, M.; Tremel, W.; Zentel, R.; Passerini, S. Extraordinary Performance of Carbon-Coated Anatase TiO_2 As Sodium-Ion Anode. *Adv. Energy Mater.* **2016**, *6*, 1501489.
(35) Chen, C.; Wen, Y.; Hu, X.; Ji, X.; Yan, M.; Mai, L.; Hu, P.; Shan, B.; Huang, Y. Na^+ Intercalation Pseudocapacitance in Graphene-Coupled Titanium Oxide Enabling Ultra-Fast Sodium Storage and Long-Term Cycling. *Nat. Commun.* **2015**, *6*, 6929.
(36) Jiang, J.; Yang, W.; Wang, H.; Zhao, Y.; Guo, J.; Zhao, J.; Beidaghi, M.; Gao, L. Electrochemical Performances of MoO_2/C Nanocomposite for Sodium Ion Storage: An Insight Into Rate Dependent Charge/Discharge Mechanism. *Electrochim. Acta* **2017**, *240*, 379−387.
(37) Augustyn, V.; Simon, P.; Dunn, B. Pseudocapacitive Oxide Materials for High-Rate Electrochemical Energy Storage. *Energy Environ. Sci.* **2014**, *7*, 1597−1614.
(38) Augustyn, V.; Come, J.; Lowe, M. A.; Kim, J. W.; Taberna, P. L.; Tolbert, S. H.; Abruna, H. D.; Simon, P.; Dunn, B. High-Rate Electrochemical Energy Storage Through Li^+ Intercalation Pseudocapacitance. *Nat. Mater.* **2013**, *12*, 518−522.
(39) Subramanian, V.; Zhu, H. W.; Vajtai, R.; Ajayan, P. M.; Wei, B. Q. Hydrothermal Synthesis and Pseudocapacitance Properties of MnO_2 Nanostructures. *J. Phys. Chem. B* **2005**, *109*, 20207−20214.
(40) Hu, Z.; Wang, L. X.; Zhang, K.; Wang, J. B.; Cheng, F. Y.; Tao, Z. L.; Chen, J. MoS_2 Nanoflowers With Expanded Interlayers As High-Performance Anodes for Sodium-Ion Batteries. *Angew. Chem., Int. Ed.* **2014**, *53*, 12794−12798.
(41) Chen, M. H.; Liang, X. Q.; Yin, J. H.; Chen, Q. G.; Xia, X. H. Graphene Foam Supported V_2O_5/N-C Core/Shell Arrays As Advanced Cathode for Lithium Ion Storage. *J. Alloys Compd.* **2018**, *735*, 2022−2029.
(42) Huang, Z.; Hou, H.; Wang, C.; Li, S.; Zhang, Y.; Ji, X. Molybdenum Phosphide: A Conversion-Type Anode for Ultralong-Life Sodium-Ion Batteries. *Chem. Mater.* **2017**, *29*, 7313−7322.
(43) Sun, R. M.; Wei, Q. L.; Sheng, J. Z.; Shi, C. W.; An, Q. Y.; Liu, S. J.; Mai, L. Q. Novel Layer-By-Layer Stacked VS_2 Nanosheets With Intercalation Pseudocapacitance for High-Rate Sodium Ion Charge Storage. *Nano Energy* **2017**, *35*, 396−404.
(44) Zhu, Y.; Peng, L. L.; Chen, D. H.; Yu, G. H. Intercalation Pseudocapacitance in Ultrathin $VOPO_4$ Nanosheets: Toward High-Rate Alkali-Ion-Based Electrochemical Energy Storage. *Nano Lett.* **2016**, *16*, 742−747.
(45) Yuan, T. Z.; Jiang, Y. Z.; Sun, W. P.; Xiang, B.; Li, Y.; Yan, M.; Xu, B.; Dou, S. X. Ever-Increasing Pseudocapacitance In RGO-Mno-RGO Sandwich Nanostructures For Ultrahigh-Rate Lithium Storage. *Adv. Funct. Mater.* **2016**, *26*, 2198−2206.
(46) Zhao, C. T.; Yu, C.; Qiu, B.; Zhou, S.; Zhang, M. D.; Huang, H. W.; Wang, B. Q.; Zhao, J. J.; Sun, X. L.; Qiu, J. S. Ultrahigh Rate and Long-Life Sodium-Ion Batteries Enabled by Engineered Surface and Near-Surface Reactions. *Adv. Mater.* **2018**, *30*, 1702486.
(47) Chao, D. L.; Zhu, C. R.; Yang, P. H.; Xia, X. H.; Liu, J. L.; Wang, J.; Fan, X. F.; Savilov, S. V.; Lin, J. Y.; Fan, H. J.; Shen, Z. X. Array of Nanosheets Render Ultrafast and High-Capacity Na-Ion Storage By Tunable Pseudocapacitance. *Nat. Commun.* **2016**, *7*, 12122.
(48) Wang, J.; Polleux, J.; Lim, J.; Dunn, B. Pseudocapacitive Contributions to Electrochemical Energy Storage in TiO_2 (Anatase) Nanoparticles. *J. Phys. Chem. C* **2007**, *111*, 14925−14931.
(49) Ma, C. R.; Zhang, W. M.; He, Y. S.; Gong, Q.; Che, H. Y.; Ma, Z. F. Carbon Coated SnO_2 Nanoparticles Anchored on CNT As A Superior Anode Material for Lithium-Ion Batteries. *Nanoscale* **2016**, *8*, 4121−4126.
(50) Huang, Y.; Gong, Q. F.; Song, X. N.; Feng, K.; Nie, K. Q.; Zhao, F. P.; Wang, Y. Y.; Zeng, M.; Zhong, J.; Li, Y. G. Mo_2C Nanoparticles Dispersed on Hierarchical Carbon Microflowers for Efficient Electrocatalytic Hydrogen Evolution. *ACS Nano* **2016**, *10*, 11337−11343.
(51) Chen, Y. Y.; Zhang, Y.; Jiang, W. J.; Zhang, X.; Dai, Z. H.; Wan, L. J.; Hu, J. S. Pomegranate-Like N,P-Doped Mo_2C@C Nanospheres As Highly Active Electrocatalysts for Alkaline Hydrogen Evolution. *ACS Nano* **2016**, *10*, 8851−8860.
(52) Cramer, S. P.; Eccles, T. K.; Kutzler, F. W.; Hodgson, K. O.; Mortenson, L. E. Letter: Molybdenum X-Ray Absorption Edge Spectra. The Chemical State Of Molybdenum In Nitrogenase. *J. Am. Chem. Soc.* **1976**, *98*, 1287−1288.
(53) Zhong, Y.; Xia, X. H.; Zhan, J. Y.; Wang, X. L.; Tu, J. P. A CNT Cocoon On Sodium Manganate Nanotubes Forming A Core/Branch Cathode Coupled With A Helical Carbon Nanofibre Anode for Enhanced Sodium Ion Batteries. *J. Mater. Chem. A* **2016**, *4*, 11207−11213.
(54) Chen, J.; Zhang, Y.; Zou, G. Q.; Huang, Z. D.; Li, S. M.; Liao, H. X.; Wang, J. F.; Hou, H. S.; Ji, X. B. Size-Tunable Olive-Like Anatase TiO_2 Coated With Carbon As Superior Anode for Sodium-Ion Batteries. *Small* **2016**, *12*, 5554−5563.
(55) Chu, C.; Yang, J.; Zhang, Q.; Wang, N.; Niu, F.; Xu, X.; Yang, J.; Fan, W.; Qian, Y. Biphase-Interface Enhanced Sodium Storage and Accelerated Charge Transfer: Flower-Like Anatase/Bronze TiO_2/C As An Advanced Anode Material for Na-Ion Batteries. *ACS Appl. Mater. Interfaces* **2017**, *9*, 43648−43656.
(56) Le, Z.; Liu, F.; Nie, P.; Li, X.; Liu, X.; Bian, Z.; Chen, G.; Wu, H. B.; Lu, Y. Pseudocapacitive Sodium Storage In Mesoporous Single-Crystal-Like TiO_2−Graphene Nanocomposite Enables High-Performance Sodium-Ion Capacitors. *ACS Nano* **2017**, *11*, 2952−2960.
(57) Li, B.; Xi, B.; Feng, Z.; Lin, Y.; Liu, J.; Feng, J.; Qian, Y.; Xiong, S. Hierarchical Porous Nanosheets Constructed By Graphene-Coated, Interconnected TiO_2 Nanoparticles for Ultrafast Sodium Storage. *Adv. Mater.* **2018**, *30*, 1705788.

DOI: 10.1021/acsnano.8b07811
ACS Nano 2019, 13, 671−680

(58) Zhang, Y.; Ding, Z.; Foster, C. W.; Banks, C. E.; Qiu, X.; Ji, X. Oxygen Vacancies Evoked Blue TiO_2(B) Nanobelts With Efficiency Enhancement in Sodium Storage Behaviors. *Adv. Funct. Mater.* **2017**, *27*, 1700856.
(59) Zhang, Y.; Wang, C.; Hou, H.; Zou, G.; Ji, X. Nitrogen Doped/Carbon Tuning Yolk-Like TiO_2 and Its Remarkable Impact on Sodium Storage Performances. *Adv. Energy Mater.* **2017**, *7*, 1600173.
(60) Takami, N.; Satoh, A.; Hara, M.; Ohsaki, T. Structural and Kinetic Characterization of Lithium Intercalation Into Carbon Anodes for Secondary Lithium Batteries. *J. Electrochem. Soc.* **1995**, *142*, 371.
(61) Ho, C.; Raistrick, I. D.; Huggins, R. A. Application of AC Techniques to The Study of Lithium Diffusion in Tungsten Trioxide Thin Films. *J. Electrochem. Soc.* **1980**, *127*, 343−350.
(62) Chen, C. J.; Wen, Y. W.; Hu, X. L.; Ji, X. L.; Yan, M. Y.; Mai, L. Q.; Hu, P.; Shan, B.; Huang, Y. H. Na^+ Intercalation Pseudocapacitance in Graphene-Coupled Titanium Oxide Enabling Ultra-Fast Sodium Storage and Long-Term Cycling. *Nat. Commun.* **2015**, *6*, 7929.
(63) Zhao, X.; Wang, H.-E.; Yang, Y.; Neale, Z. G.; MassÉ, R. C.; Cao, J.; Cai, W.; Sui, J.; Cao, G. Reversible And Fast Na-Ion Storage In MoO_2/$MoSe_2$ Heterostructures for High Energy-High Power Na-Ion Capacitors. *Energy Storage Mater.* **2018**, *12*, 241−251.
(64) Conway, B. E.; Birss, V.; Wojtowicz, J. The Role and Utilization of Pseudocapacitance for Energy Storage By Supercapacitors. *J. Power Sources* **1997**, *66*, 1−14.
(65) Lindstrom, H.; Sodergren, S.; Solbrand, A.; Rensmo, H.; Hjelm, J.; Hagfeldt, A.; Lindquist, S. E. Li^+ Ion Insertion In TiO_2 (Anatase) 0.2. Voltammetry On Nanoporous Films. *J. Phys. Chem. B* **1997**, *101*, 7717−7722.
(66) Bard, A. J.; Faulkner, L. R. *Electrochemical Methods: Fundamentals and Applications*; John Wiley & Sons: New York, 1980.
(67) Le, Z. Y.; Liu, F.; Nie, P.; Li, X. R.; Liu, X. Y.; Bian, Z. F.; Chen, G.; Wu, H. B.; Lu, Y. F. Pseudocapacitive Sodium Storage in Mesoporous Single-Crystal-Like TiO_2-Graphene Nanocomposite Enables High-Performance Sodium-Ion Capacitors. *ACS Nano* **2017**, *11*, 2952−2960.

NOTE ADDED AFTER ISSUE PUBLICATION

Zi-Feng Ma was incorrectly indicated as affiliated with Argonne National Laboratory in the version published December 28, 2018. The corrected version was published on the Web on February 6, 2019.

DOI: 10.1021/acsnano.8b07811
ACS Nano 2019, 13, 671−680